Supplementary Materials for

Observation and control of maximal Chern numbers in a chiral topological semimetal

Niels B.M. Schröter*, Samuel Stolz, Kaustuv Manna, Fernando de Juan, Maia G. Vergniory, Jonas A. Krieger, Ding Pei, Thorsten Schmitt, Pavel Dudin, Timur K. Kim, Cephise Cacho, Barry Bradlyn, Horst Borrmann, Marcus Schmidt, Roland Widmer, Vladimir N. Strocov, and Claudia Felser*

correspondence to: *niels.schroeter@psi.ch*, *claudia.felser@cpfs.mpg.de*

This PDF file includes:

Materials and Methods

PdGa Crystal Growth and Structure Refinement

PdGa single crystals were grown from its melt using the self-flux technique. First, a polycrystalline ingot was prepared using arc melt technique with the stoichiometric mixture of high purity Pd and Ga metals. Then the crushed powder was filled in a bottom-cone shaped alumina crucible and finally sealed in a quartz tube. In order to control the structural chirality of the grown PdGa single crystals, we prepared the seeds of Fe1-xCoxSi with Co doping x = 0.08 and x = 0.25 (35). Single crystals of $Fe_{1-x}Co_xSi$ [x = 0.08 and 0.25] were grown using the self-flux technique with melting the respective stoichiometric polycrystalline material at 1500 °C and followed by slow cooling to 1200 °C with a rate of 5 °C/h. We then cut off small pieces of the grown $Fe_{1-x}Co_xSi$ single crystals and used them as seeds at the bottom of the alumina crucible. For both batches of PdGa single crystals, first, the entire quartz ampoule was heated to 1100 °C, halted there for 12 h and then slowly cooled to 900 °C with a rate of 1.5 °C/h. Finally, the sample was cooled to 800 °C with a rate of 50 °C/h, annealed for 120 h and then cooled to 500 °C with a rate of 5 °C/h. For the growth of "form A" defined in Refs. (36,37), single crystal of $Fe_{1-x}Co_xSi$ with x = 0.08; and for the "form B", x = 0.25 single crystals were used as a seed. High-quality PdGa single crystals with an average dimension of about 18 mm length and 6 mm diameter were obtained.

ARPES

Soft X-ray ARPES (SX-ARPES) measurements were performed at the SX-ARPES endstation (38) of the ADRESS beamline (39) at the Swiss Light Source, Switzerland, with a SPECS analyzer with an angular resolution of 0.07°. The photon energy varied from 350-1000 eV and the combined energy resolution was ranging between 50 meV to 150 meV. The temperature during sample cleaving and measurements was about 20 K and the pressure better than $1x10^{-10}$ mbars. The increase of the photoelectron mean free path in the soft-X-ray energy range results, by the Heisenberg uncertainty principle, in a higher k_z resolution of the ARPES experiment compared to measurements at lower photon energies (40), which was critical to measure the multifold fermions in the bulk band structure of PdGa.

VUV-ARPES measurements were performed at the high-resolution ARPES branch line of the beamline I05 at the Diamond Light Source, UK (41). Measurements at the high-resolution branch were performed with a Scienta R4000 analyzer, and a photon energy range between 20 eV and 200 eV, at a temperature below 20 K. Measurements in the VUV-ARPES regime are more surface sensitive than SX-ARPES and therefore most suitable to image the Fermi-arcs in PdGa.

At both ARPES beamlines, the polished PdGa were sputtered with Ar-ions and annealed at T=870 K in UHV for multiple cycles, until clear LEED spots became visible.

Ab-initio calculations

We employed density functional theory (DFT) as implemented in the Vienna Ab Initio Simulation Package (VASP) (43,44), as well as Wien2k (45,46), but the latter only for Fig 2. D-E.

For the VASP calculations, the exchange correlation term is described according to the Perdew-Burke-Ernzerhof (PBE) prescription together with projected augmented-wave pseudopotentials (46). For the autoconsistent calculations, we used a 6x6x6 k-points mesh for the bulk and 6x6x1 for the slab calculations. The kinetic energy cut off was set to 520 eV. We calculated the surface states by using a slab geometry along the (001) direction. In order to achieve a negligible interaction between the surface states from both sides of the slab and reduce the overlap between top and bottom surface states, we considered a slab of 10-unit cells and 1 nm vacuum thickness. For the energy cuts, we used a 100x100 grid of K points.

The Wien2k calculations employed a full-potential linearized augmented plane-wave and local orbitals basis, as well as the PBE prescription of the exchange correlation term. The plane-wave cutoff parameter RMTKMAX was set to 7 and the irreducible Brillouin zone was sampled by 97,336 k-points. Spin-orbit coupling was included via a second variational procedure.

The crystal structure plotted in Fig. 1 were generated with VESTA (47).

Supplementary Text

1. PdGa Crystal Structure Refinement

Single crystallinity was first checked with a white beam backscattering Laue X-ray setup at room temperature. Then we performed rigorous single-crystal X-ray diffraction experiments to analyze the structural chirality of the grown two batches of PdGa single crystals. Small pieces picked from different parts of the grown crystals were considered to truly reflect the structural properties of the entire sample. The selected crystallites were mounted on Kapton loops with aid of a trace of Apiezon H grease and used in diffraction experiments on a Rigaku AFC7 four-circle diffractometer with a Saturn 724+ CCD-detector applying graphite-monochromatized Mo-Kα radiation. A total of five crystals were fully characterized, which were extracted from two large crystals (sample names KMa_189 and KMa_199). The determination of the absolute structure via refinement of Flack's parameter confirmed single domain crystals without any significant contribution from twinning by inversion (48, 49). A summary of the crystallographic information can be found in Table S1. It fully confirms the proper assignment of hand as expected from crystal growth. Complete crystallographic information is compiled in standard cif format and is available in Ref. (50).

2. Spin-orbit splitting of the bulk band structure around the R-point

Besides the six-fold band crossing at the R point, there should be other bands at slightly higher binding energy that are split off from the main band crossing due to spin-orbit coupling (for a comparison of ab-initio calculations with and without spin-orbit, see Refs. (16,17)). In Fig. S2 we show the raw ARPES data for the dispersion along the M-R-M and X-R-X direction, together with the second derivative spectrum of the raw ARPES data, which shows a more pronounced splitting.

3. Reversal of the Fermi-arc velocity between the two enantiomers

In Fig. 4B-C, we show that the Fermi-velocity of the Fermi-arcs that are bridging the projected band gap are reversed when considering the component along the k_y direction. The band dispersion shown in Fig. 4C not only shows the Fermi arcs that are bridging the bulk gap, but also additional bulk and surface pockets at the Fermi-level. In Fig. S3 we show the band dispersion along a curved line-cut that passes only through the projected band gap and divides the surface Brillouin zone between the projected bulk pockets at $\bar{\Gamma}$ and $\bar{R}$, as indicated by the red dashed arrows in Fig. S3A. In Fig. S3B we show the band dispersion along this curved path. Here, the numbers on the horizontal axis indicate the distance travelled on the curved path that starts at the lower end of the dashed red arrow. We can see that only two branches of Fermi-arcs are crossing the Fermi-level, which are indicated by the solid red arrows in Fig. S3B. These are the same Fermi-arcs that are indicated with the red solid arrows in Fig. 4C, which shows that the reversal of the Fermi-velocity of these bands captures – via the bulk boundary correspondence – the reversal of the Berry curvature flow between the bulk band pockets at the $\bar{\Gamma}$ and $\bar{R}$. The latter indicates a reversal of the Chern number signs when comparing two enantiomers.

4. Topological edge states at domain boundaries between two enantiomers of a chiral topological semimetal

To understand what will happen at the interface between two enantiomers, it is instructive to compare the Chern numbers of the 2D quantum Hall slices in the Brillouin zones, as illustrated as light blue shaded planes in Fig. 1D. For positive momenta, the Chern number C of the quantum Hall slice changes from C=-2 in enantiomer A to C=+2 in enantiomer B, and vice versa for negative momenta. This implies that at the domain wall boundary, there must be four topological edge states with positive momenta, and four counter-propagating edge states with negative momenta, which can also be intuitively understood from the real space llustration of glueing the top and bottom surfaces of the two enantiomers, as illustrated in Fig. S4. Due to the coupling of multifold fermions with opposite chirality at the interface, we expect that these domain walls may host topological interface states that are qualitatively different from those at the vacuum interface, which could lead to novel topological and correlated phases.

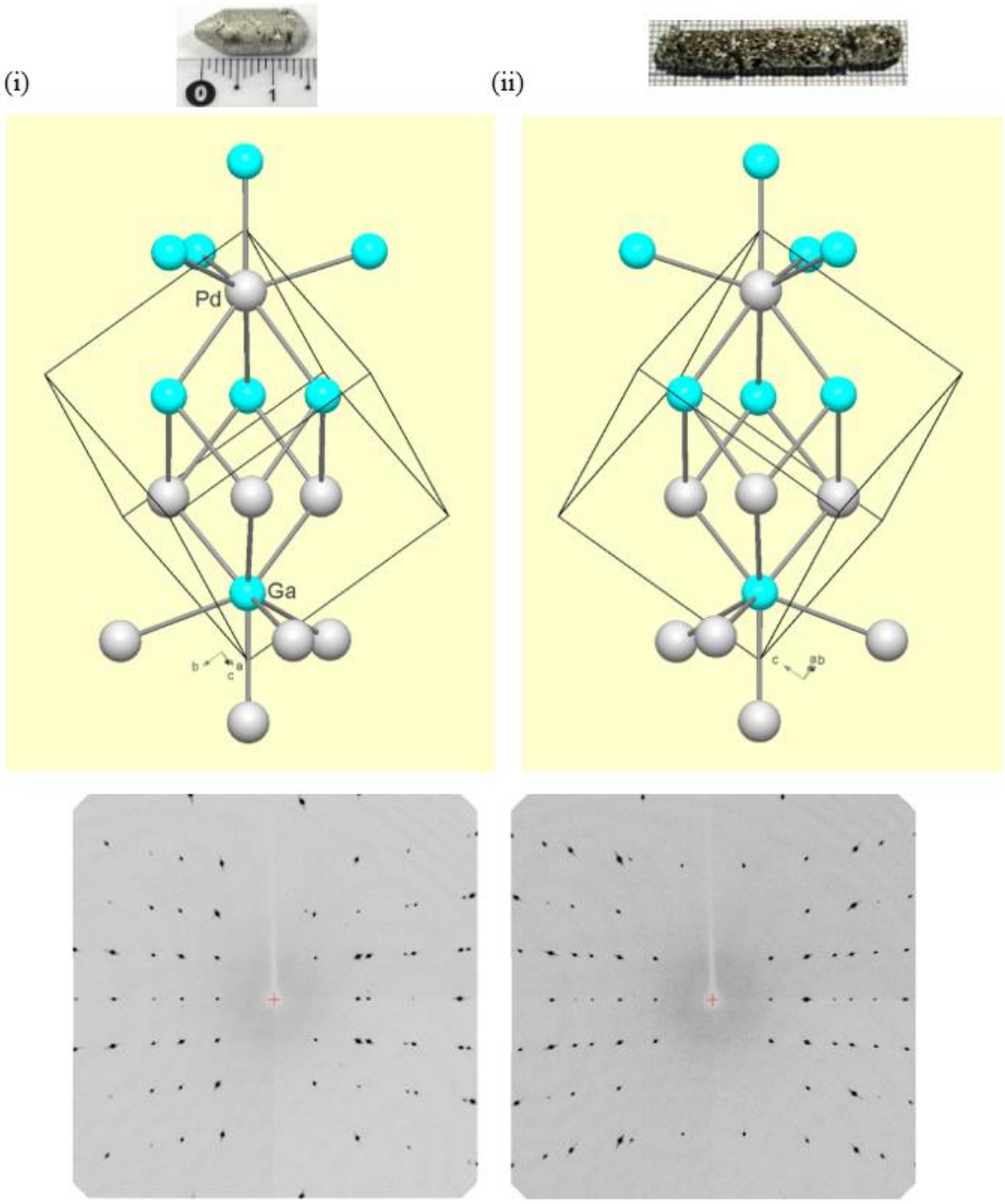

Fig. S1 Basic structural unit for the PdGa crystals with the refined structural parameters.

(i): right handed or A-form crystal as defined in Ref. (36) [Pd at x = 0.14246(4), Ga at x = 0.84301(6)] and (ii): left-handed or B-form crystal [Pd at x = 0.85758(3), Ga at x = 0.15694(5)]. The corresponding top picture shows the grown PdGa single crystal. Below are the oscillation images about a main axis for both PdGa single crystals, reflecting the excellent crystalline quality.

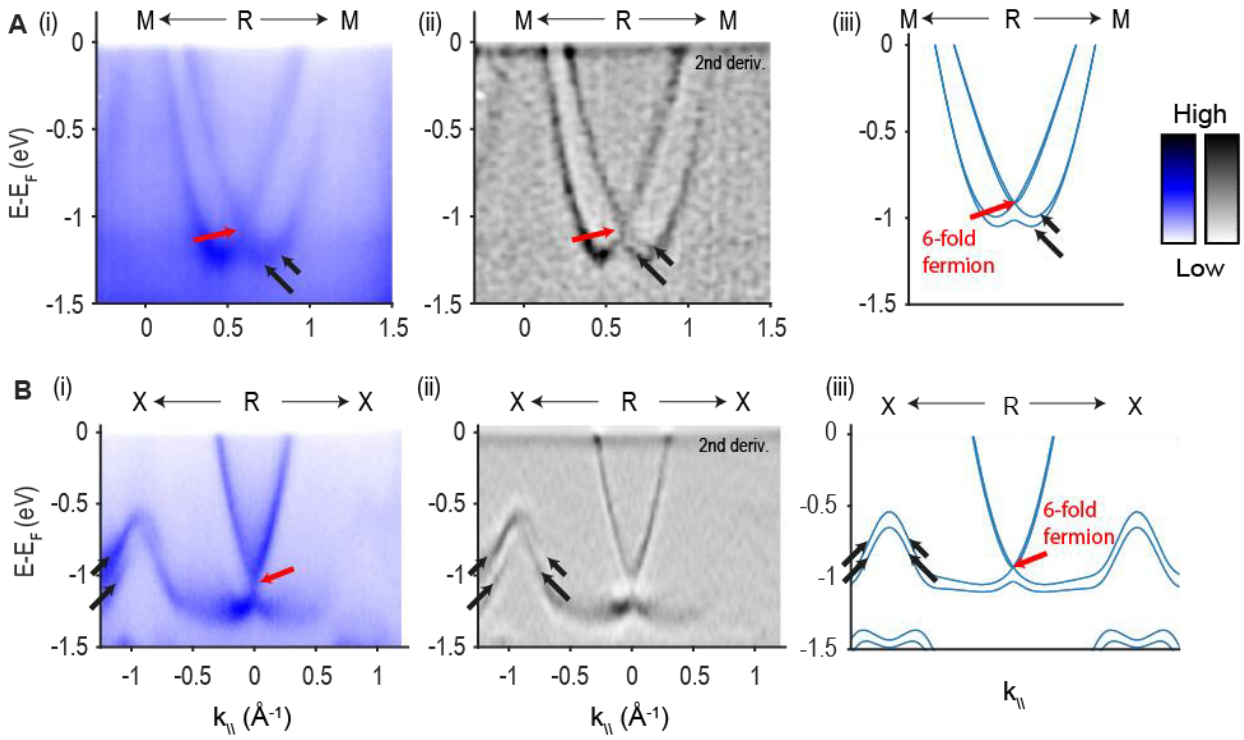

Fig. S2 Band splitting due to spin-orbit coupling near the R point

(A) (i) Experimental band dispersion along the M-R-M direction, as displayed in Fig. 2B. Red arrow indicates the band crossing at R, and the black arrows indicate the band splitting due to spin-orbit coupling. (ii) 2nd derivative plot of the data presented in (i). The black arrows indicate the band splitting. (iii) Ab-initio calculation of the band dispersion, red arrow indicates the six-fold band crossing at R, and the black arrows indicate the spin-orbit splitting.

(B) (i) Experimental band dispersion along the X-R-X direction as displayed in Fig 2A. Red arrow indicates the band crossing at R, and the black arrows indicate the band splitting due to spin-orbit coupling. (ii) 2nd derivative plot of the data presented in (i). The black arrows indicate the band splitting. (iii) Ab-initio calculation of the band dispersion, red arrow indicates the six-fold band crossing at R, and the black arrows indicate the spin-orbit splitting.

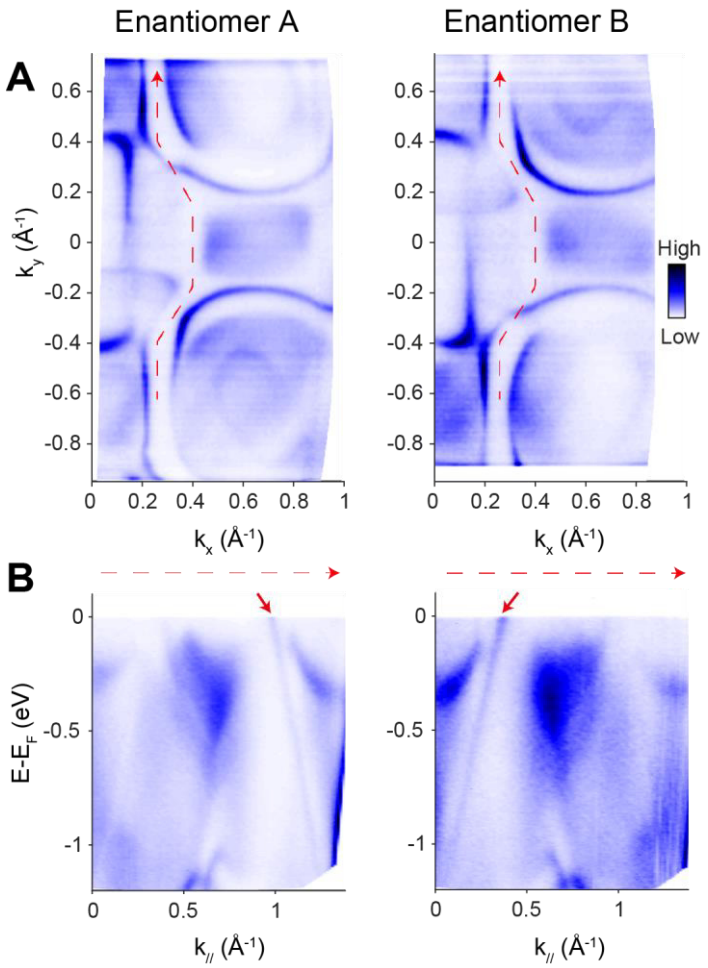

Fig. S3 Fermi-arc dispersion along a curved path.

(A) The same Fermi-surfaces that are displayed in Fig. 4 of the main manuscript. The dashed red arrow indicates the path of the line cut shown below, which is traversing through the projected bulk band gap.

(B) Band dispersion along the path indicated by the red dashed arrow in (A). The horizontal axis is the distance from the beginning of the path at the lower end of the red dashed arrow in (A).

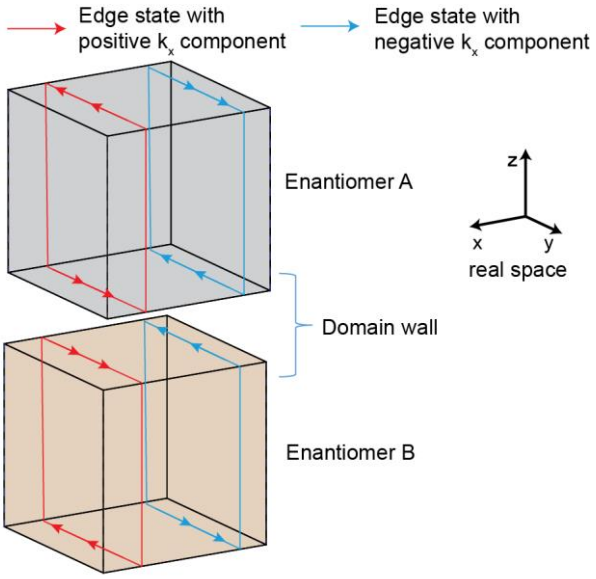

Fig. S4 Topological domain wall states at the interface between two enantiomers.
Red and blue arrows indicate the direction of their Fermi-velocity component along the y-axis.

Sample name	Pd x=y=z	Ga x=y=z	Flack parameter	Enantiomer
KMa_189am	0.14246(4)	0.84301(6)	0.020(21)	A
KMa_189b	0.14248(6)	0.84307(9)	0.032(32)	A
KMa_189cm	0.14251(3)	0.84311(5)	0.017(20)	A
KMa_199am	0.85758(3)	0.15694(5)	0.001(20)	B
KMa_199bm	0.85746(4)	0.15681(7)	0.008(24)	B

Table S1 Results from XRD structure refinement for five crystallites extracted from the samples used for ARPES and LEED measurements

Table includes positions of the Palladium (Pd) and Gallium atoms (Ga), as well as Flack factors. The atomic positions are given here with respect to a right-handed coordinate system.